Research Paper

Platelet-camouflaged nanococktail: Simultaneous inhibition of drug-resistant tumor growth and metastasis via a cancer cells and tumor vasculature dual-targeting strategy

Lijia Jing[1], Haijing Qu[1], Dongqi Wu[1], Chaojian Zhu[1], Yongbo Yang[2], Xing Jin[1], Jian Zheng[1], Xiangsheng Shi[1], Xiufeng Yan[1] and Yang Wang[1]✉

1. Center for Bioactive Products, Northeast Forestry University/Key Laboratory of Saline-Alkali Vegetation Ecology Restoration, Ministry of Education, Harbin 150040, China.
2. State Key Laboratory of Veterinary Biotechnology, Harbin Veterinary Research Institute, Chinese Academy of Agricultural Sciences, Harbin 150069, China.

✉ Corresponding author: Yang Wang, Email: ywang1971@hotmail.com

Abstract

Multidrug resistance (MDR) poses a great challenge to cancer therapy. It is difficult to inhibit the growth of MDR cancer due to its chemoresistance. Furthermore, MDR cancers are more likely to metastasize, causing a high mortality among cancer patients. In this study, a nanomedicine RGD-NPVs@MNPs/DOX was developed by encapsulating melanin nanoparticles (MNPs) and doxorubicin (DOX) inside RGD peptide (c(RGDyC))-modified nanoscale platelet vesicles (RGD-NPVs) to efficiently inhibit the growth and metastasis of drug-resistant tumors via a cancer cells and tumor vasculature dual-targeting strategy.

Methods: The *in vitro* immune evasion potential and the targeting performance of RGD-NPVs@MNPs/DOX were examined using RAW264.7, HUVECs, MDA-MB-231 and MDA-MB-231/ADR cells lines. We also evaluated the pharmacokinetic behavior and the *in vivo* therapeutic performance of RGD-NPVs@MNPs/DOX using a MDA-MB-231/ADR tumor-bearing nude mouse model.

Results: By taking advantage of the self-recognizing property of the platelet membrane and the conjugated RGD peptides, RGD-NPVs@MNPs/DOX was found to evade immune clearance and target the αvβ3 integrin on tumor vasculature and resistant breast tumor cells. Under irradiation with a NIR laser, RGD-NPVs@MNPs/DOX produced a multipronged effect, including reversal of cancer MDR, efficient killing of resistant cells by chemo-photothermal therapy, elimination of tumor vasculature for blocking metastasis, and long-lasting inhibition of the expressions of VEGF, MMP2 and MMP9 within the tumor.

Conclusion: This versatile nanomedicine of RGD-NPVs@MNPs/DOX integrating unique biomimetic properties, excellent targeting performance, and comprehensive therapeutic strategies in one formulation might bring opportunities to MDR cancer therapy.

Key words: platelet, melanin nanoparticles, drug-resistant cancer, metastasis inhibition, chemo-photothermal therapy

Introduction

Multidrug resistance (MDR) poses a great challenge to cancer therapy [1, 2]. It is difficult to inhibit the growth of MDR cancer due to its chemoresistance. Furthermore, MDR cancers are more

likely to metastasize, causing a high mortality among cancer patients [3, 4]. Therefore, there is a pressing need to develop therapies that effectively inhibit MDR cancer growth and metastasis. In recent years, nanoparticulate drugs that integrate photothermal therapy (PTT) and drug delivery have shown promise for the treatment of MDR cancers [5-8]. Nanoparticles can increase the drug accessibility of resistant cells through endocytosis-mediated cellular uptake [9-11]. In addition to the ablation of resistant cells [12], photoinduced hyperthermia can reverse MDR through the inhibition of MDR-related proteins [5, 7]. However, nanosystems accumulate at the tumor target in insufficient quantities after intravenous injection because of shielding by the protein corona in the blood and rapid immune clearance by the mononuclear phagocyte system (MPS) [13-15]. In addition, MDR cancers are more metastatic than other cancers, but current nanomedicines used for treating MDR cancer by chemo-photothermal therapy have focused only on cancer cell killing; they lack a tailored performance to inhibit the metastasis of resistant cells [5-8].

To eradicate MDR cancer through chemo-photothermal treatment, nanosystems with long blood circulation times and high tumor specificity are urgently needed to deliver an adequate dose of PTT agents and anti-cancer drugs to the same target to achieve the optimal combinatory effect. More recently, due to their "self-recognized" property, biomembranes from red blood cells, platelets, cancer cells and macrophages have been used to camouflage nanoparticles to evade immune clearance [16-32]. Among these membranes, platelet membranes have drawn much attention because of their accessibility and unique physiological functions, such as vascular damage response and recognition of and interaction with circulating tumor cells [27-32]. Such properties make platelet membranes outstanding platforms for tumor targeting. Moreover, platelet-biomimetic nanoparticles often display elongated blood circulation times and decreased absorption by healthy organs [27-32]. Therefore, platelet-derived nanocarriers with immune-evading and tumor-targeting capabilities are expected to reach their full potential in chemo-photothermal therapy for MDR cancers by maximizing the delivery of PPT agents and anti-cancer drugs to the tumor target.

In addition, the creation of advanced treatments for metastatic MDR cancer requires an understanding of the development process of these cancers. It has been documented that the tumor vasculature can act as a pathway for both nutrients and cancer metastasis [33, 34]. From the viewpoint of killing resistant cells, it can be advantageous to target the tumor vasculature,

invoking the well-known "starvation effect" [35, 36]. Meanwhile, blocking MDR cancer metastasis can also be achieved by the elimination of the tumor vasculature [37]. Taken together, strategies that simultaneously target resistant cells and the tumor vasculature are highly advantageous for the effective inhibition of MDR cancer growth and metastasis. In this study, we designed a novel nanomedicine by encapsulating melanin nanoparticles (MNPs) and doxorubicin (DOX) inside RGD peptide (c(RGDyC))-modified nanoscale platelet vesicles (RGD-NPVs). Melanin, a natural and safe biopolymer, has been used for medical imaging, drug delivery and PTT targeting cancer [38-41]. Herein, MNPs combined with DOX were used for safe chemo-photothermal therapy. The usage of RGD-NPVs as carriers imparted the therapeutic agent with immune-evading capabilities and facilitated the targeting of the agent to the αvβ3 integrin. After intravenous administration, RGD-NPVs@MNPs/DOX can simultaneously target the tumor vasculature and the resistant cells to implement the chemo-photothermal elimination of resistant cells and tumor vasculature via irradiation with a NIR laser, resulting in an efficient inhibition of the growth and metastasis of MDR cancer.

Results and discussion

Preparation and characterization of RGD-NPVs@MNPs/DOX

As demonstrated in **Figure 1A**, RGD-NPVs@MNPs/DOX was fabricated by encapsulating MNPs using RGD-NPVs, followed by loading DOX inside RGD-NPVs@MNPs. Hydrophilic MNPs with a size of 3.8 ± 0.68 nm were extracted from *Auricularia auricula* (**Figure 1B**). In the FTIR spectra of the MNPs (**Figure S1**), the bending vibrations of the aromatic C=C, C=N and C=O groups (1600-1700 cm^{-1}) and the stretching vibration of the -OH group (3450 cm^{-1}) were observed, indicating that the MNPs were rich in the aromatic indole and pyrrole ring structures necessary for photothermal conversion and binding of DOX through π–π interactions. Platelet membrane (PM) extracted from fresh platelets is shown in **Figure S2**. A BCA protein assay demonstrated that the obtained PM contained approximately 14.1 wt.% of membrane proteins (data not shown), and thus the RGD peptide could be coupled to the PM surface via linkage with PM proteins. The linkage between the RGD peptides and the PM proteins is generally random; thus, functional proteins may be inactivated by changes in the functional domain caused by RGD peptide conjugation. Therefore, to construct RGD-NPVs@MNPs/DOX, the fused PM and RGD-PM were used to avoid the complete invalidation of PM proteins. To

fabricate the RGD-NPVs@MNPs, 2 mg of the fused PM and RGD-PM and 6 mg of MNPs were dispersed in 1 mL of PBS buffer. An increase of MNP input increases the viscosity of the suspension, making it difficult to be homogenized and extruded. By loading MNPs, RGD-NPVs@MNPs can load with DOX through π–π interactions by a simple incubation. After purification, the UV-vis-NIR spectrum of RGD-NPVs@MNPs/DOX displayed the characteristic absorptions of DOX and MNPs, indicating the successful encapsulation of MNPs and DOX (**Figure S3**). The loading contents of DOX and MNPs were respectively determined to be 7.6 ± 0.8 wt.% and 32.7 ± 1.9 wt.%. The corresponding encapsulation efficiencies of DOX and MNPs were respectively calculated to be 70.6 ± 5.9 wt.% and 18.3 ± 0.9 wt.%.

TEM imaging revealed that the obtained RGD-NPVs@ MNPs/DOX exhibited a spherical morphology with dense dark spots inside (**Figure 1C**). The hydrodynamic particle size of RGD-NPVs@MNPs/ DOX was evaluated to be 85.92 ± 6.28 nm, which was favorable for achieving the EPR effect in tumor vasculature. For RGD-NPVs@MNPs/DOX, the surface charge was evaluated to be -23.5 ± 2.6 mV (**Figure S4**), comparable to that of PM (-24.5 ± 3.1 mV) and RGD-PM (-22.8 ± 3.2 mV). In addition, SDS-PAGE was performed on RGD-NPVs@MNPs/DOX, PM and RGD-PM. (**Figure 1D**). It was found that RGD-NPV s@MNPs/DOX contained endogenous membrane proteins preserved by PM and RGD-PM. Our results indicated the good completeness of PM after the nanoparticle construction.
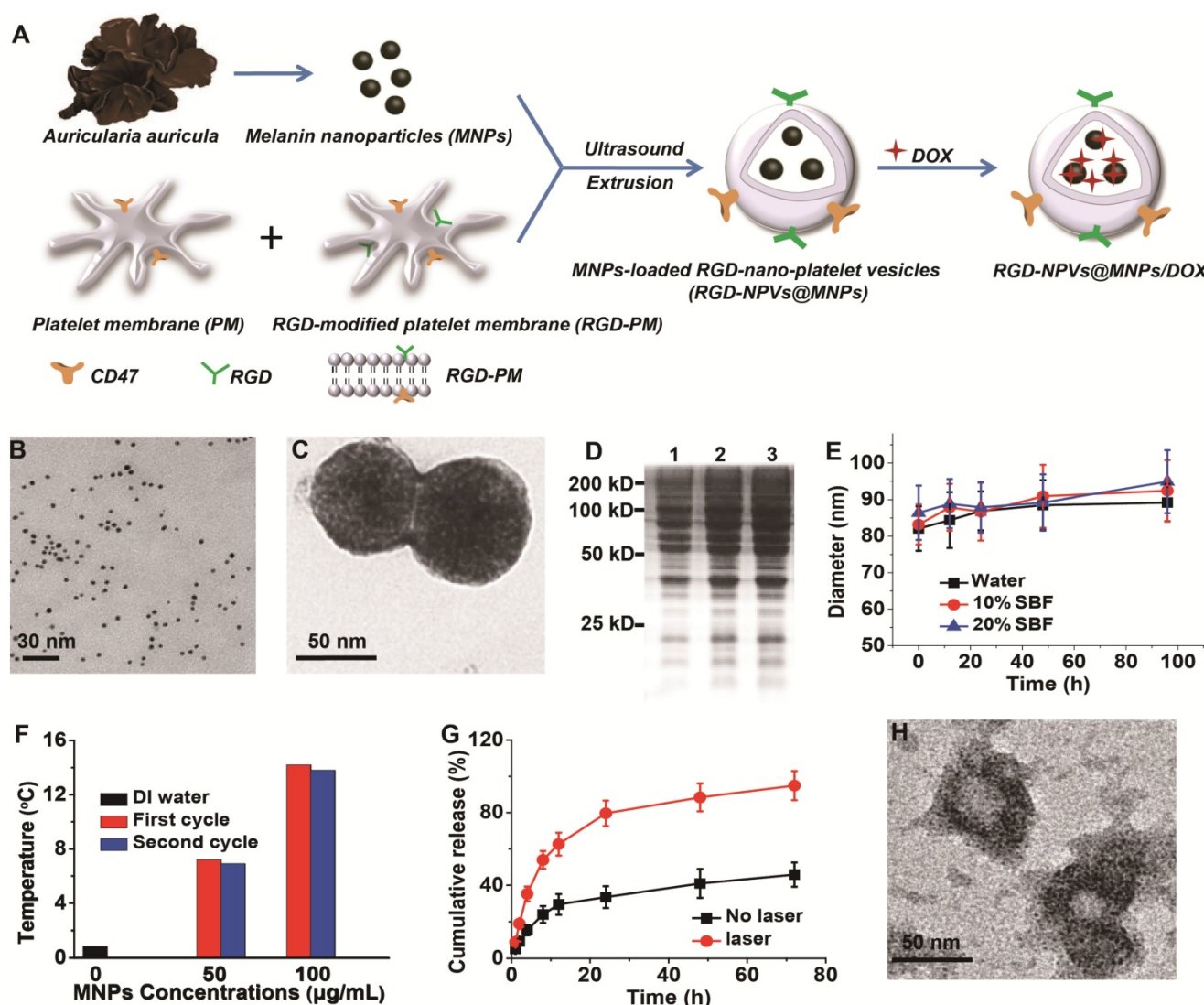

Figure 1. (A) Fabrication process and structural illustration of RGD-NPVs@MNPs/DOX. **(B)** TEM image of MNPs. **(C)** TEM image of RGD-NPVs@MNPs/DOX. **(D)** SDS-PAGE protein analysis of (1) RGD-NPVs@MNPs/DOX, (2) RGD-PM and (3) PM. **(E)** Time-dependent colloidal stability of RGD-NPVs@MNPs/DOX in water, 10% SBF and 20% SBF solutions at 37 °C. **(F)** Temperature elevations of DI water and RGD-NPVs@MNPs/DOX with MNP concentrations of 50 μg/mL and 100 μg/mL over a period of 10 min of exposure to the NIR laser (808 nm, 1.5 W). **(G)** *In vitro* release behavior of DOX from RGD-NPVs@MNPs/DOX with or without NIR laser irradiation (808 nm, 1.5 W, 10 min). **(H)** TEM image of RGD-NPVs@MNPs/DOX after treatment with the NIR laser (808 nm, 1.5 W, 10 min).

Photothermal behavior and drug release profile of RGD-NPVs@MNPs/DOX

As shown in **Figure 1E**, RGD-NPVs@MNPs/DOX displayed excellent colloidal stability in water and in simulated body fluid (SBF) solutions (pH 7.4) without any significant changes in particle size for 96 h at 37 °C. After NIR laser irradiation (808 nm, 1.5 W, and 10 min), the temperature was only increased by 0.82 °C for DI water (**Figure 1F**). In contrast, well-repeated temperature elevations of approximately 7 °C and 14 °C were achieved after two cycles of NIR laser irradiation of RGD-NPVs@MNPs/DOX when the MNP concentration was 50 µg/mL and 100 µg/mL, respectively. This result demonstrated the excellent photothermal efficiency and photostability of RGD-NPVs@MNPs/DOX. The drug release profiles of RGD-NPVs@MNPs/DOX were investigated in 10% SBF solution (pH 7.4) at 37 °C. As illustrated in **Figure 1G**, without laser treatment, RGD-NPVs@MNPs/DOX displayed a long-lasting release profile of DOX in the simulated environment (nearly 45% within 72 h), which, in practice, would ensure a high drug accumulation in the tumor tissue, although it may take time for cancer cells to uptake the nanoagents. In stark contrast, a DOX release greater than 90% was achieved within 72 h when RGD-NPVs@MNPs/DOX was treated with a one-time irradiation by NIR laser (800 nm, 1.5 W, 10 min). Revealed by TEM imaging (**Figure 1H**), a "melting effect" occurred on RGD-NPVs@MNPs/DOX after treatment with the NIR laser. This finding suggests that the photothermal effect of RGD-NPVs@MNPs/DOX itself can trigger the release of DOX by melting the PM. In addition, the dependence of the drug release on laser power was investigated by treating RGD-NPVs@MNPs/DOX with increased laser power for the same irradiation period of 10 min (**Figure S5**). Compared with the nearly 53% DOX release under a 1.5 W NIR laser, the DOX release observed within 8 h reached nearly 73.6% and 86.7% with a laser power of 2.4 W and 3.6 W, respectively. This NIR laser-responsive drug release is greatly beneficial for reducing side effects and enhancing the effectiveness of chemotherapy at the tumor site.

Immune evasion potential and targeting performance of RGD-NPVs@MNPs/DOX

The immune evasion potential of RGD-NPVs@MNPs/DOX was illustrated through the incubation with mouse macrophage RAW264.7 cells. Commercial injectable lipid (DPPC)-based nanovesicles encapsulating MNPs and DOX (NLVs@MNPs/DOX) were used for comparison. Both RGD-NPVs@MNPs/DOX and NLVs@MNPs/DOX were labeled with RhB by doping the same amount of DOPE-RhB during the nanoparticle construction. Thus, the cellular uptake of these two NPs could be investigated through the evaluation of intracellular fluorescence. Fluorescence images showed that at the same NP concentration (50 µg/mL), the uptake of RGD-NPVs@MNPs/DOX by RAW264.7 cells was significantly suppressed compared to that of NLVs@MNPs/DOX at 4 h post-incubation (**Figure 2A**). A further quantitative analysis using fluorescence spectroscopy indicated a nearly 67.5% reduction of the intracellular fluorescence intensity of RhB in RGD-NPVs@MNPs/DOX-treated cells (**Figure 2B**). This result demonstrated the evasive ability of RGD-NPVs@MNPs/DOX, which may be attributed to the specific immunomodulatory effect of the PM proteins [27-29]. The targeting ability of RGD-NPVs@MNPs/DOX was investigated *in vitro* in comparison with that of NPVs@MNPs/DOX (RGD-free NPs). Herein, human umbilical vein endothelial cells (HUVECs), human breast cancer cells (MDA-MB-231) and DOX-resistant cells (MDA-MB-231/ADR; overexpression of P-gp) were tested, and all the cells expressed the αvβ3 integrin (**Figure 2C**). To make the two NPs easily detectable, they were labeled with RhB. The intracellular number of NPs was quantified by fluorescence spectroscopy at 4, 8 and 12 h post-incubation. As seen in **Figure S6**, both NPVs@MNPs/DOX and RGD-NPVs@MNPs/DOX were increasingly internalized by the test cells in a time-dependent manner. In all the tested cell types, compared to the low fluorescence intensity observed in cells treated with NPVs@MNPs/DOX, the RGD-NPVs@MNPs/DOX group exhibited much higher fluorescence intensity (**Figure S6**). A competitive binding experiment was also performed by incubating the cells with RGD-NPVs@MNPs/DOX in the presence of an excess amount of free RGD peptides (**Figure S6**). It was found that the free RGD peptides significantly diminished the intracellular uptake of RGD-NPVs@MNPs/DOX by all the tested cell types. This phenomenon was likely attributed to the competitive binding of free RGD peptides to the αvβ3 integrin. Thus, our results indicated that RGD peptides can significantly improve the targeting ability of NPVs@MNPs/DOX, and the specific targeting to the αvβ3 integrin may enable a simultaneous targeting effect to cancer cells and tumor vasculature.

In vitro therapeutic performance of RGD-NPVs@MNPs/DOX

Before evaluating the therapeutic potential of RGD-NPVs@MNPs/DOX, the biocompatibility of RGD-NPVs and MNPs was investigated (**Figure

S7-8). It was found that both RGD-NPVs and MNPs exhibited almost no toxicity to any of the test cells, indicating the reliable biosafety of these nanoparticles. The chemotherapeutic potential of RGD-NPVs@MNPs/DOX was investigated in comparison with NPVs@MNPs/DOX and free DOX. As shown in **Figure 2D**, due to the multidrug resistance, free DOX had an IC50 value of 161.3 ± 9.98 µg/mL against MDA-MB-231/ADR cells for 24 h, which was increased nearly 14-fold compared to the IC50 value

against MDA-MB-231 cells (11.31 ± 0.68 µg/mL). In our study, RGD-NPVs@MNPs/DOX exhibited a higher chemotherapeutic activity than that of free DOX and NPVs@MNPs/DOX against all the tested cells. For RGD-NPVs@MNPs/DOX after 24 h of incubation, the IC50 values against HUVECs, MDA-MB-231 and MDA-MB-231/ADR cells were 3.28 ± 0.98, 2.62 ± 0.45 and 3.95 ± 0.69 µg/mL, respectively, which were lower than the IC50 values for NPVs@MNPs/DOX and free DOX.
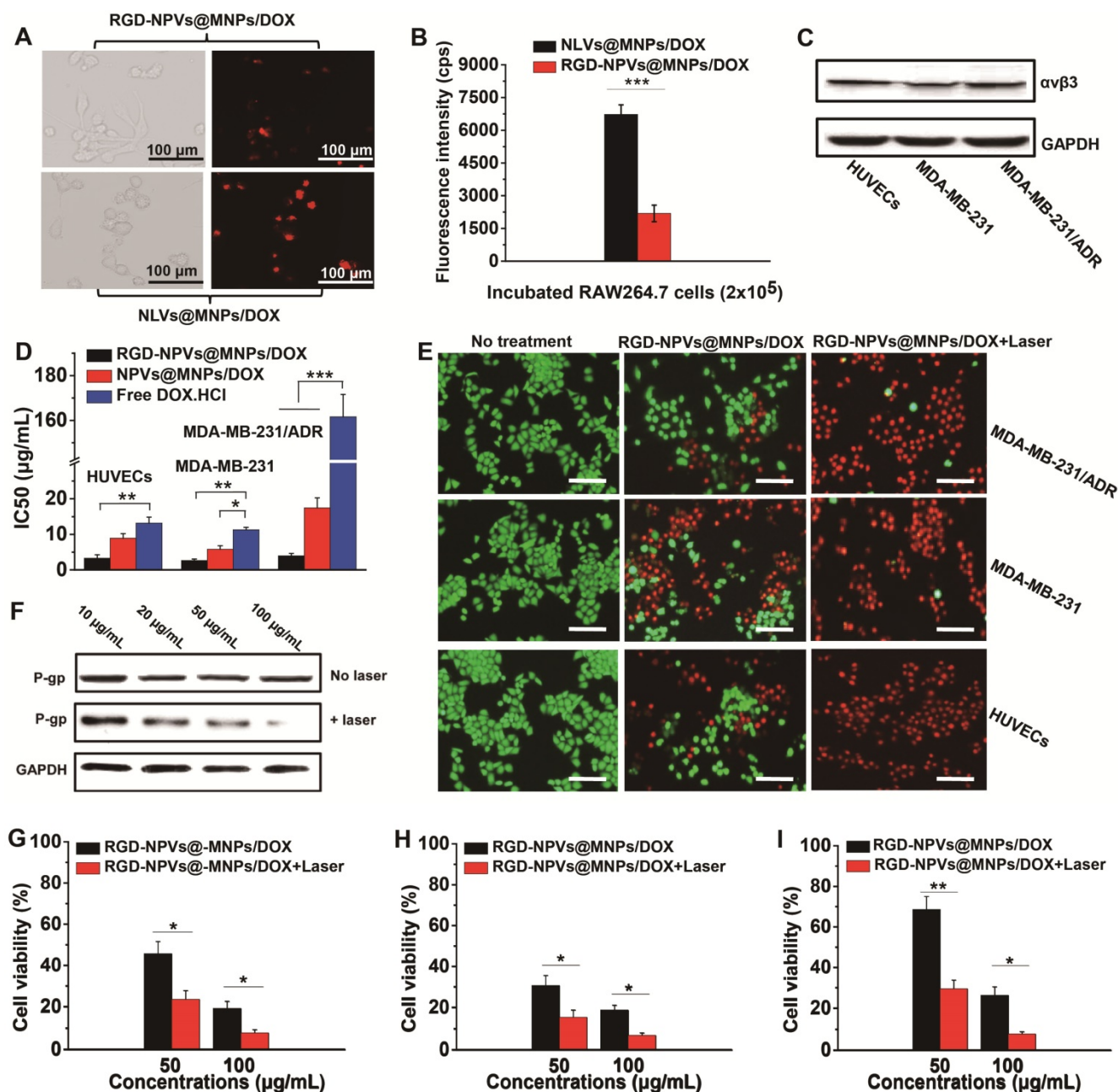

Figure 2. (A) Fluorescence images and **(B)** fluorescence intensities of RAW264.7 cells after incubation with RhB-labeled RGD-NPVs@MNPs/DOX and NLVs@MNPs/DOX at a concentration of 50 µg/mL for 4 h. **(C)** Western blot analysis of αvβ3 integrin expression for different cells. **(D)** IC50 values of HUVECs, MDA-MB-231 and MDA-MB-231/ADR cells after treatment with different formulations for 24 h. **(E)** Fluorescence images of HUVECs, MDA-MB-231 and MDA-MB-231/ADR cells stained with Calcein AM and PI after treatment with RGD-NPVs@MNPs/DOX only and RGD-NPVs@MNPs/DOX + laser at an NP concentration of 100 µg/mL (red signal, dead cells; green signal, live cells). Scale bar represents 200 µm. **(F)** Western blot analysis of the P-gp levels in MDA-MB-231/ADR cells after treatment with RGD-NPVs@MNPs/DOX only and RGD-NPVs@MNPs/DOX + laser for 4 h. Viability of HUVECs **(G)**, MDA-MB-231 cells **(H)** and MDA-MB-231/ADR cells **(I)** after treatment with RGD-NPVs@MNPs/DOX only and RGD-NPVs@MNPs/DOX + laser at NP concentrations of 50 µg/mL and 100 µg/mL. *, $P < 0.05$; **, $P < 0.01$; ***, $P < 0.001$.

Remarkably, the IC50 value for RGD-NPVs@MNPs/DOX against MDA-MB-231/ADR cells was only 1.5-fold higher than that against MDA-MB-231 cells, which may be attributed to the combination of the active targeting and the endocytosis-mediated cellular uptake of RGD-NPVs@MNPs/DOX. Due to the high-efficiency active targeting, RGD-NPVs@MNPs (drug-free agent) exhibited higher photothermal cytotoxicity relative to free MNPs and NPVs@MNPs (**Figure S9**). Under the same MNP concentration (100 µg/mL) and NIR laser conditions (1.5 W cm^{-2}, 10 min), RGD-NPVs@MNPs decreased the viability of HUVECs, MDA-MB-231 and MDA-MB-231/ADR cells to nearly 36%, 39% and 44% respectively, at 24 h post-irradiation. These cell survival rates were lower than those observed from NPVs@MNPs and free MNPs. Western blotting, MTT assay and calcein AM/PI staining were used to investigate the photothermal-chemotherapeutic potential of RGD-NPVs@MNPs/DOX. As shown in **Figure 2F**, without laser irradiation, the expression of P-gp in MDA-MB-231/ADR cells treated with RGD-NPVs@MNPs/DOX at various concentrations did not show any obvious changes at 4 h post-incubation. In contrast, RGD-NPVs@MNPs/DOX was found to remarkably inhibit the expression of P-gp in a dose-dependent manner under light irradiation (1.5 W cm^{-2}, 10 min), suggesting that the hyperthermia generated from the photothermal effect of RGD-NPVs@MNPs/DOX could sensitize resistant cells to chemotherapeutic drugs by suppressing the resistance pathway. Both the results of calcein AM/PI staining and the MTT assay showed that the photothermal-chemotherapeutic treatment of RGD-NPVs@MNPs/DOX could increase the inhibition rate on the MDA-MB-231, MDA-MB-231/ADR and HUVECs cells compared with chemotherapy alone (**Figure 2E, G-I**). Further study showed that the outcome from the photothermal-chemotherapeutic treatment of RGD-NPVs@MNPs/DOX depends on the laser strength and irradiation time (**Table S2**). Excitingly, RGD-NPVs@MNPs/DOX exhibited nearly the same inhibiting effect against both MDA-MB-231 and MDA-MB-231/ADR cells at an adequate dosage, laser strength and irradiation time (**Figure 2H-I** and **Table S2**). All the results indicated that RGD-NPVs@MNPs/DOX could effectively overcome drug resistance via NIR laser irradiation, possibly due to multipronged effects, including enhanced cell internalization, light-triggered drug release and photothermal-mediated inhibition of P-gp.

Pharmacokinetic behavior of RGD-NPVs@MNPs/DOX.

To confirm whether PM could improve the circulation profile of the NPs, the blood circulation dynamics of RGD-NPVs@MNPs/DOX and NPVs@MNPs/DOX were investigated in comparison with NLVs@MNPs/DOX. All the NPs were labeled with RhB at the same mass ratio and intravenously injected into MDA-MB-231/ADR tumor-bearing mice at 100 mg/kg. As shown in **Figure 3A**, NLVs@MNPs/DOX underwent rapid elimination from the blood circulation in mice. In contrast, RGD-NPVs@MNPs/DOX and NPVs@MNPs/DOX displayed remarkably prolonged retention in the blood circulation. As seen in **Table S3**, the blood half-life (T$_{1/2}$), mean residence time (MRT) and area under the plasma concentration-time curve from zero to time infinity (AUC$_{0-\infty}$) of RGD-NPVs@MNPs/DOX were calculated as 26.4 ± 3.2 h, 34.62 ± 5.71 h and 5,983.37 ± 659.46 h µg/L, respectively, which were similar to those of NPVs@MNPs/DOX (T$_{1/2}$ of 27.6 ± 4.1 h, MRT of 36.89 ± 7.46 h and AUC$_{0-\infty}$ of 6,398.42 ± 973.28 h µg/L) but significantly higher than those of NLVs@MNPs/DOX (T$_{1/2}$ of 5.13 ± 2.61 h, MRT of 7.79 ± 3.23 h and AUC$_{0-\infty}$ of 726.21 ± 298.4 h µg/L). To further understand the pharmacokinetic behaviors of the NPs, NIR fluorescence imaging of the tumor-bearing mice was performed after the intravenous injection of the NPs (**Figure 3B** and **Figure S10**). The distribution of fluorescence intensity indicated that NLVs@MNPs/DOX accumulated primarily in the lung, liver and spleen and could not effectively accumulate in the tumor, as the fluorescence intensity in tumor tissues was nearly unchanged after 6 h. This rapid clearance of NLVs@MNPs/DOX by the lung, liver and spleen may be ascribed to the trapping by phagocytes in these organs. This result is consistent with our *in vitro* study, in which NLVs@MNPs/DOX was captured at a high rate by mouse macrophage RAW264.7 cells (**Figure 2A-B**). In comparison, RGD-NPVs@MNPs/DOX and NPVs@MNPs/DOX displayed a relatively lower accumulation in the lung, liver and spleen but a gradually increased accumulation in the tumor during the 24 h post-injection. This finding indicated that PM could slow down the clearance rate of RGD-NPVs@MNPs/DOX and NPVs@MNPs/DOX. It is worth noting that RGD-NPVs@MNPs/DOX exhibited significantly enhanced tumor affinity compared with NPVs@MNPs/DOX. This effective tumor affinity was attributed to the optimal combination of immune evasion and RGD peptide-mediated active targeting. Immunofluorescent staining of tumor sections was used to further investigate the affinity behavior of RGD-NPVs@MNPs/DOX to tumor tissue. The CD31 immunofluorescent staining results illustrated that RGD-NPVs@MNPs/DOX could target tumor vessels more efficiently than NPVs@MNPs/DOX could at only 4 h post-injection (**Figure 3C**). At 24 h post-injection,

RGD-NPVs@MNPs/DOX was distributed more widely than NPVs@MNPs/DOX in the tumor tissue (**Figure 3D**). Our results confirmed the strong ability of RGD-NPVs@MNPs/DOX to target tumor neovasculature and cancer cells *in vivo*.

In vivo therapeutic performance of RGD-NPVs@MNPs/DOX

Based upon the encouraging results of the tumor affinity and the *in vitro* antitumor activity of RGD-NPVs@MNPs/DOX, an MDA-MB-231/ADR tumor model was used to investigate the therapeutic performance of RGD-NPVs@MNPs/DOX *in vivo*. RGD-NPVs@MNPs/DOX, NPVs@MNPs/DOX and free DOX were injected into tumor-bearing mice through the caudal vein. For all formulations, the same DOX dosage of 10 mg/kg was used. In that case, the MNP dosage for the NPVs@MNPs/DOX group was nearly equivalent to that of the RGD-NPVs@MNPs/DOX group (~43 mg/kg). As shown in **Figure 4A**, free DOX exhibited almost no

inhibition of tumor growth, due to the drug resistance, whereas RGD-NPVs@MNPs/DOX and NPVs@MNPs/DOX suppressed the tumor growth to different degrees. Compared with the NPVs@MNPs/DOX-treated group, a more obvious MDR reversal by solo chemotherapy was achieved in the RGD-NPVs@MNPs/DOX-treated group, which was likely due to the RGD peptide-mediated targeted intracellular drug delivery. The photothermal-chemotherapeutic treatment was implemented by irradiating the tumors with an NIR laser (1.5 W cm^{-2}, 10 min) at 24 h post-injection. Compared with the nearly unchanged tumor temperature in the laser-only treated mice (**Figure S11**), the tumor temperature was elevated approximately 9.4 and 16.7 °C for the NPVs@MNPs/DOX and RGD-NPVs@MNPs/DOX-treated mice, respectively, resulting in the levels of tumor ablation shown in **Figure 4B**. Compared with the PBS-injected group, the tumor volume in the NPVs@MNPs/DOX + laser group increased to only ~173 mm^3 within 22 days. Remarkably, the tumor
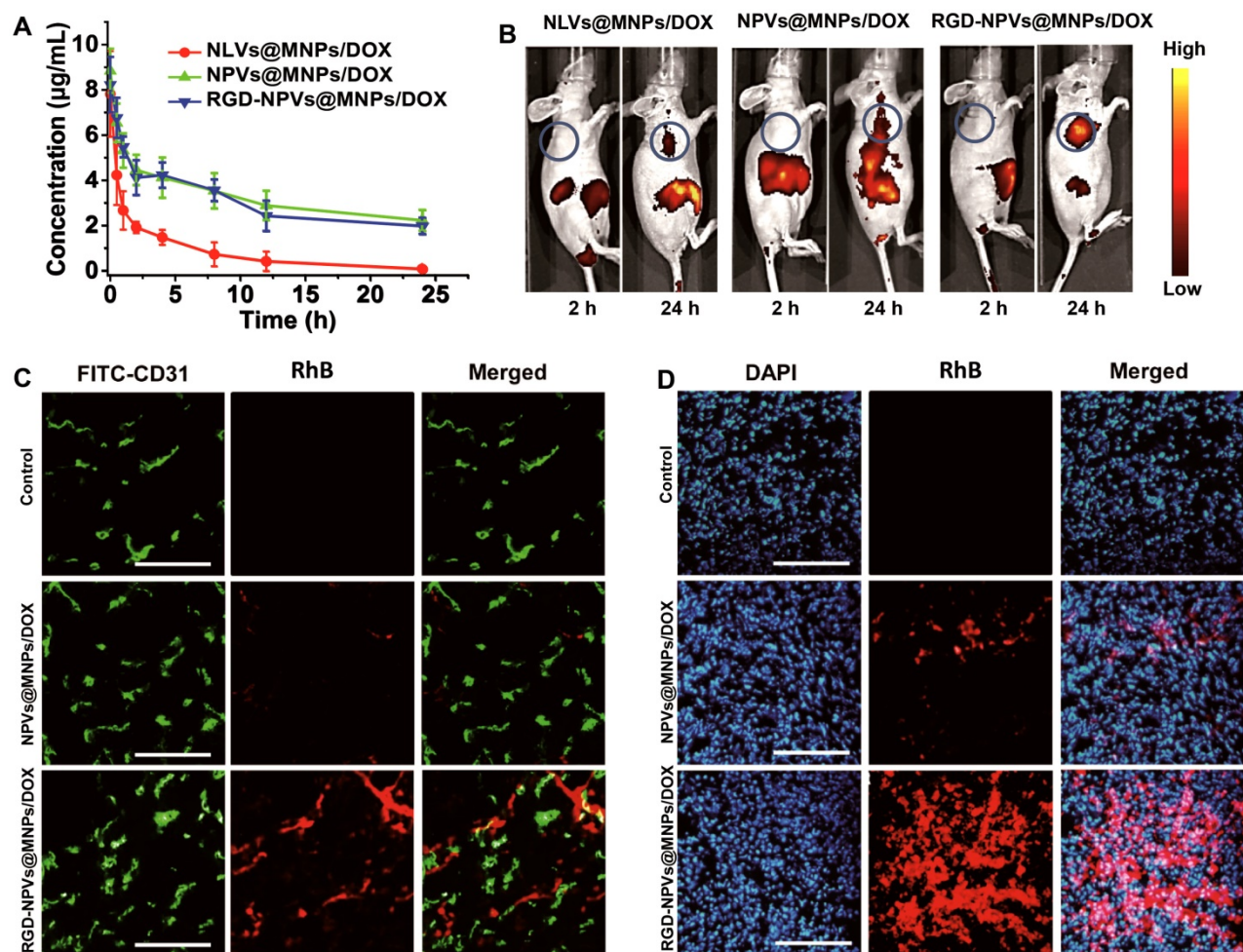

Figure 3. (A) Circulation time of NLVs@MNPs/DOX, NPVs@MNPs/DOX and RGD-NPVs@MNPs/DOX in mice bearing MDA-MB-231/ADR tumors. **(B)** Fluorescence images of mice bearing MDA-MB-231/ADR tumors at 2 h and 24 h after intravenous injection of NLVs@MNPs/DOX, NPVs@MNPs/DOX and RGD-NPVs@MNPs/DOX. Frozen sections of MDA-MB-231/ADR tumors at 4 h **(C)** and 24 h **(D)** after intravenous injection of NPVs@MNPs/DOX and RGD-NPVs@MNPs/DOX. A FITC-tagged CD31 antibody was used to label the tumor vasculature, and DAPI was used to label the nuclei (red signal, RhB; blue signal, DAPI; green signal, FITC). Scale bar represents 300 µm.

volume in the mice treated with RGD-NPVs@MNPs/DOX in combination with the laser was decreased to 20 mm³, indicating a more efficient inhibition of tumor growth. Obvious metastatic nodules were found in the lungs of the mice treated with PBS, DOX and NPVs@MNPs/DOX (**Figure 4D-F**). In contrast, the RGD-NPVs@MNPs/DOX and NPVs@MNPs/DOX + laser treatments interfered with metastasis to varying degrees. Excitingly, RGD-NPVs@MNPs/DOX in combination with laser treatment completely inhibited the metastasis of MDA-MB-231/ADR tumors to the lung. Immunofluorescent staining and gene expression tests were used to further investigate the significant inhibition of growth and metastasis observed in the RGD-NPVs@MNPs/DOX + laser group.
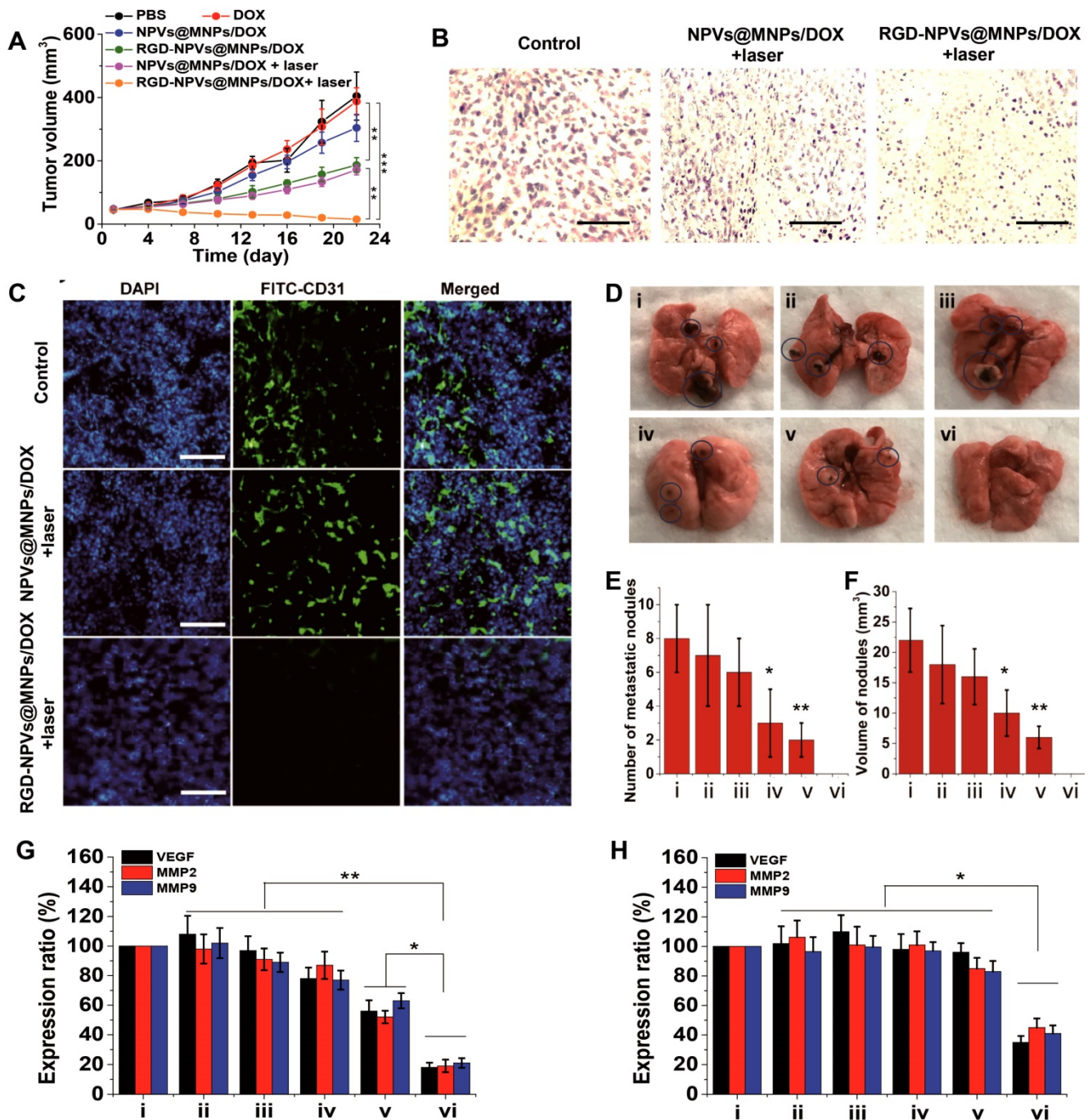

Figure 4. (A) The tumor growth curves of different groups. **(B)** Representative histological sections of tumors from mice at 2 days after the various treatments. Scale bar represents 200 µm. **(C)** Frozen sections of tumors at 2 days after the various treatments. A FITC-tagged CD31 antibody and DAPI were used to label the tumor vasculature and nuclei, respectively (blue signal, DAPI; green signal, FITC). Scale bar represents 300 µm. **(D)** Representative images of the lung tissues at 22 days after the various treatments. **(E)** Number and **(F)** volume of metastatic nodules in lung tissues at 22 days after the treatments. i) PBS; ii) DOX; iii) NPVs@MNPs/DOX; iv) RGD-NPVs@MNPs/DOX; v) NPVs@MNPs/DOX + laser; vi) RGD-NPVs@MNPs/DOX + laser. The expression levels of VEGF, MMP2 and MMP9 in tumor tissues at **(G)** 2 h and **(H)** 22 days after the treatments. i) PBS; ii) DOX; iii) NPVs@MNPs/DOX; iv) RGD-NPVs@MNPs/DOX; v) NPVs@MNPs/DOX + laser; vi) RGD-NPVs@MNPs/DOX + laser. *, P < 0.05; **, P < 0.01; ***, P < 0.001.

Staining with DAPI revealed obvious destruction of the nuclei in the tumors treated with RGD-NPVs@MNPs/DOX + laser; however, this trend was less prevalent in the group that received the NPVs@MNPs/DOX + laser treatment (**Figure 4C**), indicating that the RGD-NPVs@MNPs/DOX + laser treatment resulted in a more efficient tumor ablation. This finding was in agreement with the results of the H&E staining (**Figure 4B**). In addition, due to its strong ability to target tumor neovasculature, RGD-NPVs@MNPs/DOX can more effectively eliminate the tumor vascular system, in comparison with NPVs@MNPs/DOX, under NIR laser irradiation. The elimination of the vascular system blocks the pathway of tumor nutrients and cancer metastasis. Moreover, the real-time PCR results revealed that RGD-NPVs@MNPs/DOX in combination with the laser could inhibit the expression of VEGF (promotes tumor growth and angiogenesis), MMP2 and MMP9 (both are metastasis-relevant genes) in the long term more effectively than other treatments. This phenomenon may also account for the effective inhibition of metastasis and growth of MDA-MB-231/ADR tumors using RGD-NPVs@MNPs/DOX in combination with NIR laser in this study.

Biosafety evaluation

The biosafety of RGD-NPVs@MNPs/DOX was investigated. Compared with untreated mice, no apparent change in body weight and no histological injury in the main organs (liver, heart, spleen, lung, and kidney) were observed in the RGD-NPVs@ MNPs/DOX-injected mice (**Figure S12-13**). The hematology analysis results showed that the measured parameters in the RGD-NPVs@MNPs/ DOX-injected mice were nearly unchanged compared with the untreated mice (**Table S4**). Overall, the preliminary results confirmed that RGD-NPVs@M NPs/DOX was not noticeably toxic to nude mice. However, it should be noted that platelet proteins are usually immunogenic constructs, and thus many issues associated with platelet-derived nanomedicine, especially the *in vivo* immunogenicity, should be fully investigated.

Conclusion

A versatile platelet-camouflaged nanococktail of RGD-NPVs@MNPs/DOX has been designed and successfully used to inhibit the growth and metastasis of drug-resistant breast cancer through a cancer cells and tumor vasculature dual-targeting strategy. By taking advantage of the self-recognizing property of PM and the conjugation of RGD peptides, RGD-NPVs@MNPs/DOX can evade immune

clearance and sufficiently target the αvβ3 integrin, which is overexpressed on tumor vasculature and resistant breast tumor cells. Under irradiation with an NIR laser, RGD-NPVs@MNPs/DOX can implement a chemo-photothermal elimination of resistant breast tumor cells and tumor vasculature, which produces a multipronged effect, including the reversal of cancer MDR for efficient killing of resistant cells, the elimination of tumor vasculature for blocking cancer nutrients and metastasis, as well as the long-lasting inhibition of the expression of VEGF, MMP2 and MMP9. This exciting comprehensive treatment can effectively inhibit the growth and metastasis of MDR breast cancer. Taken together, these results indicate that RGD-NPVs@MNPs/DOX is a potential therapeutic platform for treating MDR breast cancers due to its unique biomimetic properties, excellent targeting performance and the multi-target and comprehensive therapeutic outcome.

Methods

Materials

RGD peptide (c(RGDyC)) was obtained from GL Biochem Ltd. (Shanghai, China). Doxorubicin was obtained from Beijing Huafeng United Technology Co. MTT, calcein-AM, propidium iodide (PI), prostaglandin E1 and Sulfo-SMCC were purchased from Sigma-Aldrich. 1,2-dipalmitoyl-sn-glycero-3-phosphocholine (DPPC) and 1,2-dioleoyl-sn-glycero-3-phosphoethanolamine-N-(Lissamine rhodamine B sulfonyl) (DOPE-RhB, excitation/emission = 560/583 nm) were purchased from Avanti Polar Lipids. All other chemicals and reagents were of analytical grade. De-ionized water (18.2 MΩ cm) from a Milli-Q purification system was used in all preparations.

Preparation of melanin nanoparticles (MNPs)

A total of 10 g of *Auricularia auricula* was added into 100 mL of 5 N HCl aqueous solution, followed by heating at 100 °C under vigorous stirring. After stirring for 8 h, a black precipitate was obtained by centrifugation at 4,500 ×g. After washing with DI water several times, the black precipitate was added into 100 mL of 0.1 N NaOH aqueous solution, followed by ultrasonication for 60 min to obtain an aqueous solution of MNPs. The MNPs were precipitated under an acidic condition and purified by dialysis in DI water. Finally, the purified MNPs were obtained after lyophilization.

Extraction and surface modification of platelet membrane (PM)

First, fresh mouse blood was anti-coagulated with EDTA and repeatedly centrifuged at 100 ×g (15 min per centrifugation) at 4 °C to prepare

platelet-containing plasma. Next, the platelet-containing plasma was mixed with phosphate buffered solution (PBS) (containing 1 mM of EDTA, 2 mM of prostaglandin E1 and protease inhibitor) and centrifuged at 800 ×g for 20 min at 4 °C to harvest the platelets. To extract the PM, the platelet suspension was frozen at -80 °C and then thawed at room temperature. After several freeze-thaw cycles, the PM was harvested by centrifugation at 4,000 ×g for 5 min and washed several times with PBS buffer containing protease inhibitor. For the RGD peptide conjugation, 100 mg of PM was added into 5 mL of carbonate buffer solution (pH = 8.0) containing 5 mg of fresh Sulfo-SMCC and protease inhibitor. After vortexing for 10 min, the thiol-active PM was retrieved using filters (100 kDa MWCO, Millipore). The thiol-activated PM was dispersed into 3 mL of RGD peptide solution (10 mM in pH 7.4 PBS). After vortexing for 20 min, the final product of RGD-modified PM was obtained using filters.

Fabrication of RGD-NPVs@MNPs/DOX

A total of 1.5 mg of PM, 0.5 mg of RGD-PM and 6 mg of MNPs were mixed in 1 mL of PBS buffer containing protease inhibitor. The mixture was vortexed for 5 min and then homogenized by sonication for 2 min at an output power of 100 W. Afterwards, the mixture was extruded through 50 nm pores repeatedly, and the MNP-loaded RGD-nanoplatelet vesicles (RGD-NPVs@MNPs) were purified by centrifugation at 1,2000 ×g to remove excess MNPs. For drug loading, 10 mg of DOX was first dispersed in 10 mL of PBS buffer and then homogenized by sonication for 20 min. Afterwards, 100 mg of RGD-NPVs@MNPs was added into the DOX solution, and the mixture was mechanically stirred at room temperature for 6 h. Finally, RGD-NPVs@MNPs/ DOX was obtained using filters (100 kDa MWCO, Millipore). The loading content of DOX was measured by a LUMINA fluorescence spectrophotometer (Thermo Scientific) and calculated according to the following equation: (total DOX used - DOX in supernatant) / RGD-NPVs@MNPs/DOX × 100%. The loading content of MNPs in RGD-NPVs@MNPs/DOX was calculated from its absorption at 650 nm (no absorption of DOX at 650 nm) using the corresponding standard calibration curve of MNPs solution.

Fabrication of NPVs@MNPs/DOX and NLVs@MNPs/DOX

The processes for fabricating NPVs@MNPs/ DOX and NLVs@MNPs/DOX were similar to the process for fabricating RGD-NPVs@MNPs/DOX. To fabricate NPVs@MNPs/DOX, PM alone was used. To fabricate NLVs@MNPs/DOX, the same amount of DPPC was used to replace the mixture of PM and RGD-PM.

Characterization of nanoparticles

The morphology of the nanoparticles at various stages was visualized by transmission electron microscopy (TEM). The size distributions and zeta potentials of the nanoparticles were evaluated using a 90Plus/BI-MAS instrument (Brookhaven Instruments Co., U.S.A.). The UV/Vis absorption spectra and the Fourier transform infrared (FTIR) spectra were measured with a Varian 4000 UV-Vis spectrophotometer and a Varian 3000 FTIR spectrophotometer, respectively. The membrane proteins of PM, RGD-PM and RGD-NPVs@MNPs/DOX were analyzed by SDS-PAGE.

Photothermal investigation of RGD-NPVs@MNPs/DOX

RGD-NPVs@MNPs/DOX formulations containing various amounts of MNPs were suspended in 3.0 mL of DI water and irradiated by an 808 nm continuous-wave NIR laser (STONE Laser, China) for 10 min. The temperature rise was recorded with a digital thermometer during the irradiation period.

Drug release

To investigate the drug release behaviors, 5 mg of RGD-NPVs@MNPs/DOX was suspended in 2 mL of PBS buffer (pH = 7.4). The suspension was sealed in a dialysis bag and immersed in 50 mL of the same PBS buffer at 37 °C with moderate stirring, and then it was exposed or not exposed to the NIR laser. At regular time intervals, 1 mL of the dialysate was removed to measure the concentration of DOX, and 1 mL of the same fresh PBS buffer was added. The concentration of DOX was measured with a LUMINA fluorescence spectrophotometer (Thermo Scientific).

Cell culture and tumor model

Mouse macrophage RAW264.7 cells, human umbilical vein endothelial cells (HUVECs), human breast cancer cells (MDA-MB-231) and DOX-resistant cells (MDA-MB-231/ADR) were cultured in DMEM medium (HyClone, Thermo Scientific, US) containing 10% FBS at 37 °C with 5% CO_2. Female BALB/c nude mice were purchased from Beijing Vital River Laboratories. MDA-MB-231/ADR tumors were generated by injecting 5×10^5 cells into the back of each mouse. All animal procedures were in agreement with institutional animal use and care committee and carried out ethically and humanely.

Cellular uptake and cytotoxicity

The cellular uptake of the NPs was evaluated. To make the NPs easily detectable, RGD-NPVs@MNPs/DOX, NPVs@MNPs/DOX and NLVs@MNPs/DOX were labeled with RhB by doping the same amount of DOPE-RhB during the nanoparticle construction. To investigate the immune evasion potential of PM, RAW264.7 cells were incubated with RhB-labeled RGD-NPVs@MNPs/DOX and NLVs@MNPs/DOX. After 4 h of incubation, RAW264.7 cells were washed with PBS buffer and observed under a fluorescence microscope. For further quantitative analysis, the incubated cells were digested and counted. The intracellular fluorescence intensity of the NPs was determined with a fluorescence spectrophotometer. To investigate the targeting efficiency of RGD-NPVs@MNPs/DOX, HUVECs, MDA-MB-231 and MDA-MB-231/ADR cells were incubated with NPVs@MNPs/DOX (RGD-free NPs), RGD-NPVs@MNPs/DOX and RGD-NPVs@MNPs/DOX + free RGD. After 4, 8, 12 h of incubation, the incubated cells were digested and counted. The intracellular fluorescence intensity of the NPs was determined with a fluorescence spectrophotometer. To investigate the chemotherapeutic cytotoxicity, HUVECs, MDA-MB-231 and MDA-MB-231/ADR cells were incubated with RGD-NPVs@MNPs/DOX, NPVs@MNPs/DOX and free DOX. After 24 h, the cell viability was measured by the standard MTT method at a wavelength of 490 nm. To investigate the solo photothermal cytotoxicity of RGD-NPVs@MNPs/DOX, HUVECs, MDA-MB-231 and MDA-MB-231/ADR cells were incubated with RGD-NPVs@MNPs (drug free agent), MNPs and NPVs@MNPs. After 4 h of incubation, the cells were washed with PBS buffer three times and exposed to the NIR laser. After 24 h, the cell viability was measured by the standard MTT method. To investigate the chemo-photothermal cytotoxicity of RGD-NPVs@MNPs/DOX, HUVECs, MDA-MB-231 and MDA-MB-231/ADR cells were incubated with RGD-NPVs@MNPs/DOX. After 4 h of incubation, the cells were washed with PBS buffer three times and exposed to the NIR laser. After 24 h, the cell viability was measured by calcein AM/PI double staining and the standard MTT method.

Western blotting for investigating the MDR reversal efficiency

MDA-MB-231/ADR cells were incubated with RGD-NPVs@MNPs/DOX. After 4 h of incubation, the cells were irradiated with or without the NIR laser (1.5 W cm^{-2}) for 10 min. At 4 h post-irradiation, the cells were washed and collected. The total cell protein was extracted using a protein extraction kit (KEYGEN, China). The protein concentration was determined with a BCA protein assay. The extracted proteins were separated using 12% SDS-PAGE electrophoresis and transferred onto polyvinylidene fluoride (PVDF) membranes (Bio-Rad). After a 1 h blocking step with 5% skim milk, the membrane was incubated with the primary antibody against P-gp (Abcam) overnight at 4 °C, and then the membrane was incubated with the secondary antibody for 1 h at room temperature. The resulting bands were visualized using an ECL-plus detection system (GE Healthcare).

In vivo pharmacokinetic and targeting performance study

Mice bearing MDA-MB-231/ADR tumors (18-20 g) were randomly divided into 3 groups (n = 6) and injected with RhB-labeled RGD-NPVs@MNPs/DOX, NPVs@MNPs/DOX or NLVs@MNPs/DOX through the caudal vein. A blood sample from each mouse was harvested from the orbital sinus at various time points and analyzed for the fluorescence intensity of RhB (excitation/emission = 560/583 nm). The fluorescence intensity of the blood sample was normalized to that of the initial injection dose of RhB-labeled nanoparticles and used to calculate the concentration of RhB-labeled nanoparticles. The NIR fluorescence images from the mice were acquired at 2 and 24 h post-injection. Time-dependent biodistribution studies were carried out by sacrificing the mice at various time points. The heart, liver, spleen, lung, kidney and tumor were harvested and analyzed for fluorescence intensity. Standard immunohisto-chemistry was used to investigate the targeting performance of RGD-NPVs@MNPs/DOX in comparison with NPVs@MNPs/DOX. Tumors were harvested and frozen in optimum cutting temperature compound (OCT). Cryosections of frozen tumor tissues were obtained using a cryostat microtome (Leica CM1950, Germany). The tumor microvascu-lature was stained with a rat anti-CD31 antibody overnight at 4 °C, followed by staining with a FITC-conjugated goat anti-rat IgG secondary antibody for 1 h. The cell nuclei were stained with DAPI. The affinity of RGD-NPVs@MNPs/DOX for cancer cells and tumor vessels was evaluated using an inverted fluorescence microscope.

In vivo tumor therapy

Mice bearing MDA-MB-231/ADR tumors (18-20 g) were randomly divided into 6 groups (n = 6) and administered PBS, DOX, NPVs@MNPs/DOX, RGD-NPVs@MNPs/DOX, NPVs@MNPs/DOX + laser, or RGD-NPVs@MNPs/DOX + laser. For the injection groups, each mouse was intravenously administered 200 µL of aqueous solution of NPs or free drugs. For

the irradiation groups, the NIR laser irradiation was implemented by an 808 nm continuous-wave diode NIR laser at 1.5 W cm^{-2} for 10 min. A thermometer probe was inserted into the tumor to dynamically record the temperature of the tumor. After the treatments, the tumor volume and diameter were measured and calculated according to the following formula: tumor volume = (tumor length) × (tumor width)^2 / 2. Tumors in the NPVs@MNPs/DOX + laser group and the RGD-NPVs@MNPs/DOX+laser group were collected after the laser treatment for an investigation of the tumor ablation by H&E staining and standard immunohistochemistry. After the treatments, the mice were sacrificed, and then the lungs were immediately excised for an analysis of the number and volume of metastatic nodules in each lung. The volume of metastatic nodule was acquired by incising the metastatic nodule from the lung, measuring the length and width using a high-precision electronic vernier caliper, and finally calculating the volume according to the formula: length × width^2 / 2.

Gene expression analysis

Genes including MMP-9, MMP-2 and VEGF were analyzed. Total RNA was extracted from fresh tumor tissues using TRIzol (Invitrogen, USA) according to the manufacturer's protocol. Next, cDNA was synthesized using the high-capacity cDNA Reverse Transcription kit (Invitrogen, USA). Real-time PCR reactions were performed using the 7500 Real-Time PCR system (Applied Biosystems, USA). Glyceraldehyde 3-phosphate dehydrogenase (GAPDH) was used as an internal control.

Toxicology evaluations

Healthy mice were used to evaluate the toxicology of RGD-NPVs@MNPs/DOX by intravenous injection of RGD-NPVs@MNPs/DOX (equal to the treatment dose). Several mice were sacrificed and subjected to a blood biochemistry assay after the injection of RGD-NPVs@MNPs/DOX. The major organs, including liver, heart, kidney, spleen, and lung, were collected at various time points and analyzed for histopathological changes after H&E staining.

Statistical analysis.

All data in the manuscript were statistically analyzed using Micorcal™ Origin 8.0 (Microcal Software). The results were compared using one-way analysis of variance (ANOVA) (*$p < 0.05$, **$p < 0.01$ and ***$p < 0.001$).

Abbreviations

MDR: multidrug resistance; PTT: photothermal therapy; NIR: near-infrared; DOX: doxorubicin; EDTA: ethylene diamine tetraacetic acid; PBS: phosphate buffered solution; SBF: simulated body fluid; PM: platelet membranes; NPVs: nanoscale platelet vesicles; RGD-NPVs: c(RGDyC) peptide modified nanoscale platelet vesicles; P-gp: p-glycoprotein; MNPs: melanin nanoparticles; DPPC: 1,2-dipalmityol-sn-glycero-3-phosphocholine; DOPE-RhB: 1,2-dioleoyl-sn-glycero-3-phosphoethanol-amine-N-(Lissamine rhodamine B sulfonyl); Sulfo-SMCC: sulfosuccinimidyl-4-(N-maleimido-methyl)cyclohexane-1-carboxylate; HUVECs: human umbilical vein endothelial cells; MPS: mononuclear phagocyte system; MRT: mean residence time; AUC: area under the plasma concentration-time curve.

Supplementary Material

Acknowledgements

Competing Interests

The authors have declared that no competing interest exists.

References

1. Coley HM. Mechanisms and strategies to overcome chemotherapy resistance in metastatic breast cancer. Cancer Treat Rev. 2008; 34: 378-90.
2. Holohan C, Van Schaeybroeck S, Longley DB, Johnston PG. Cancer drug resistance: an evolving paradigm. Nat Rev Cancer. 2013; 13: 714-26.
3. Colone M, Calcabrini A, Toccacieli L, Bozzuto G, Stringaro A, Gentile M, Cianfriglia M, Ciervo A, Caraglia M, Budillon A, Meo G, Arancia G, Molinari A. The multidrug transporter P-glycoprotein: a mediator of melanoma invasion? J Invest Dermatol. 2008; 128: 957-71.
4. Yang JM, Xu Z, Wu H, Zhu H, Wu X, Hait WN. Overexpression of extracellular matrix metalloproteinase inducer in multidrug resistant cancer cells. Mol Cancer Res. 2003; 1: 420-7.
5. Lee SM, Kim HJ, Kim SY, Kwon MK, Kim S, Cho A, Yun M, Shin JS, Yoo KH. Drug-loaded gold plasmonic nanoparticles for treatment of multidrug resistance in cancer. Biomaterials. 2014; 35: 2272-82.
6. Wang L, Lin X, Wang J, Hu Z, Ji Y, Hou S, Zhao Y, Wu X, Chen C. Novel insights into combating cancer chemotherapy resistance using a plasmonic nanocarrier: enhancing drug sensitivity and accumulation simultaneously with localized mild photothermal stimulus of femtosecond pulsed laser. Adv Funct Mater. 2014; 24: 4229-39.
7. Li Y, Deng Y, Tian X, Ke H, Guo M, Zhu A, Yang T, Guo Z, Ge Z, Yang X, Chen H. Multipronged design of light triggered nanoparticles to overcome cisplatin resistance for efficient ablation of resistant tumor. ACS Nano. 2015, 9: 9626-37.
8. Wang T, Wang D, Yu H, Wang M, Liu J, Feng B, Zhou F, Yin Q, Zhang Z, Huang Y, Li Y. Intracellularly acid-switchable multifunctional micelles for

combinational photo/chemotherapy of the drug-resistant tumor. ACS Nano. 2016, 10: 3496-508.

9. Gao Y, Chen Y, Ji X, He X, Yin Q, Zhang Z, Shi J, Li Y. Controlled intracellular release of doxorubicin in multidrug-resistant cancer cells by tuning the shell-pore sizes of mesoporous silica nanoparticles. ACS Nano. 2011; 5: 9788-98.

10. Yan Y, Björnmalm M, Caruso F. Particle carriers for combating multidrug-resistant cancer. ACS Nano. 2013; 7: 9512-7.

11. Li Y, Xu X, Zhang X, Li Y, Zhang Z, Gu Z. Tumor-specific multiple stimuli-activated dendrimeric nanoassemblies with metabolic blockade surmount chemotherapy resistance. ACS Nano. 2017; 11: 416-29.

12. Wang C, Xu L, Liang C, Xiang J, Peng R, Liu Z. Immunological responses triggered by photothermal therapy with carbon nanotubes in combination with anti-CTLA-4 therapy to inhibit cancer metastasis. Adv Mater. 2014; 26: 8154-62.

13. Torchilin VP. Recent advances with liposomes as pharmaceutical carriers. Nat Rev Drug Discov. 2005; 4: 145-60.

14. Salvati A, Pitek AS, Monopoli MP, Prapainop K, Bombelli FB, Hristov DR, Kelly PM, Åberg C, Mahon E, Dawson KA. Transferrin-functionalized nanoparticles lose their targeting capabilities when a biomolecule corona adsorbs on the surface. Nat Nanotechnol. 2013; 8: 137-43.

15. Sun H, Su J, Meng Q, Yin Q, Chen L, Gu W, Zhang P, Zhang Z, Yu H, Wang S, Li Y. Cancer-cell-biomimetic nanoparticles for targeted therapy of homotypic tumors. Adv Mater. 2016; 28: 9581-88.

16. Copp JA, Fang RH, Luk BT, Hu CM, Gao W, Zhang K, Zhang L. Clearance of pathological antibodies using biomimetic nanoparticles. Proc Natl Acad Sci USA. 2014; 111: 13481-6.

17. Tan S, Wu T, Zhang D, Zhang Z. Cell or cell membrane-based drug delivery systems. Theranostics. 2015; 5: 863-81.

18. Zhang P, Liu G, Chen X. Nanobiotechnology: cell membrane-based delivery systems. Nano Today. 2017; 13: 7-9.

19. Rao L, Cai B1, Bu LL, Liao QQ, Guo SS, Zhao XZ, Dong WF, Liu W. Microfluidic electroporation-facilitated synthesis of erythrocyte membrane-coated magnetic nanoparticles for enhanced imaging-guided cancer therapy. ACS Nano. 2017; 11: 3496-3505.

20. Chen WS, Zeng K, Liu H, Ouyang J, Wang LQ, Liu Y, Wang H, Deng L, Liu YN. Cell membrane camouflaged hollow prussian blue nanoparticles for synergistic photothermal-/chemotherapy of cancer. Adv Funct Mater. 2017; 27: 1605795.

21. Zhu JY, Zheng DW, Zhang MK, Yu WY, Qiu WX, Hu JJ, Feng J, Zhang XZ. Preferential cancer cell self-recognition and tumor self-targeting by coating nanoparticles with homotypic cancer cell membranes. Nano Lett. 2016; 16: 5895-901.

22. Chen Z, Zhao P, Luo Z, Zheng M, Tian H, Gong P, Gao G, Pan H, Liu L, Ma A, Cui H, Ma Y, Cai L. Cancer cell membrane-biomimetic nanoparticles for homologous-targeting dual-modal imaging and photothermal therapy. ACS Nano. 2016; 10: 10049-57.

23. Li SY, Cheng H, Xie BR, Qiu WX, Zeng JY, Li CX, Wan SS, Zhang L, Liu WL, Zhang XZ. Cancer cell membrane camouflaged cascade bioreactor for cancer targeted starvation and photodynamic therapy. ACS Nano. 2017; 11: 7006-18.

24. Rao L, Bu LL, Cai B, Xu JH, Li A, Zhang WF, Sun ZJ, Guo SS, Liu W, Wang TH, Zhao XZ. Cancer cell membrane-coated upconversion nanoprobes for highly specific tumor imaging. Adv Mater. 2016; 28: 3460-6.

25. Rao L, Bu LL, Xu JH, Cai B, Yu GT, Yu X, He Z, Huang Q, Li A, Guo SS, Zhang WF, Liu W, Sun ZJ, Wang H, Wang TH, Zhao XZ. Red blood cell membrane as a biomimetic nanocoating for prolonged circulation time and reduced accelerated blood clearance. Small. 2015; 11: 6225-36.

26. Rao L, Meng QF, Bu LL, Cai B, Huang Q, Sun ZJ, Zhang WF, Li A, Guo SS, Liu W, Wang TH, Zhao XZ. Erythrocyte membrane-coated upconversion nanoparticles with minimal protein adsorption for enhanced tumor imaging. ACS Appl Mater Interfaces. 2017; 9: 2159-68.

27. Hu CM, Fang RH, Wang KC, Luk BT, Thamphiwatana S, Dehaini D, Nguyen P, Angsantikul P, Wen CH, Kroll AV, Carpenter C, Ramesh M, Qu V, Patel SH, Zhu J, Shi W, Hofman FM, Chen TC, Gao W, Zhang K, Chien S, Zhang L. Nanoparticle biointerfacing by platelet membrane cloaking. Nature. 2015; 526:118-21.

28. Hu Q, Sun W, Qian C, Wang C, Bomba HN, Gu Z. Anticancer platelet-mimicking nanovehicles. Adv Mater. 2015; 27:7043-50.

29. Rao L, Bu LL, Meng QF, Cai B, Deng WW, Li A, Li KY, Guo SS, Zhang WF, Liu W, Sun ZJ, Zhao XZ. Antitumor platelet-mimicking magnetic nanoparticles. Adv Funct Mater. 2017; 27:1604774.

30. Wang C, Sun WJ, Ye YQ, Hu QY, Bomba HN, Gu Z. In situ activation of platelets with checkpoint inhibitors for post-surgical cancer immunotherapy. Nat Biomed Eng. 2017; 1: 0011.

31. Hu Q, Qian C, Sun W, Wang J, Chen Z, Bomba HN, Xin H, Shen Q, Gu Z. Engineered nanoplatelets for enhanced treatment of multiple myeloma and thrombus. Adv Mater. 2016; 28: 9573-80.

32. Hu Q, Sun W, Qian C, Bomba HN, Xin H, Gu Z. Relay drug delivery for amplifying targeting signal and enhancing anticancer efficacy. Adv Mater. 2017; 29: 1605803.

33. Folkman J. Tumor angiogenesis: therapeutic implications. N Engl J Med. 1971; 285: 1182-6.

34. Liotta LA, Steeg PS, Stetler-Stevenson WG. Cancer metastasis and angiogenesis: an imbalance of positive and negative regulation. Cell. 1991; 64:327-36.

35. Marx J. Angiogenesis. A boost for tumor starvation. Science. 2003; 301: 452-4.

36. Zhang C, Ni D, Liu Y, Yao H, Bu W, Shi J. Magnesium silicide nanoparticles as a deoxygenation agent for cancer starvation therapy. Nat Nanotechnol. 2017; 12: 378-86.

37. Zhu Y, Zhu R, Wang M, Wu B, He X, Qian Y, Wang S. Anti-metastatic and anti-angiogenic activities of core–shell SiO$_2$@LDH loaded with etoposide in non-small cell lung cancer. Adv Sci. 2016; 3:1600229.

38. Fan Q, Cheng K, Hu X, Ma X, Zhang R, Yang M, Lu X, Xing L, Huang W, Gambhir SS, Cheng Z. Transferring biomarker into molecular probe: melanin nanoparticle as a naturally active platform for multimodality imaging. J Am Chem Soc. 2014; 136: 15185-94.

39. Zhang R, Fan Q, Yang M, Cheng K, Lu X, Zhang L, Huang W, Cheng Z. Engineering melanin nanoparticles as an efficient drug-delivery system for imaging-guided chemotherapy. Adv Mater. 2015; 27: 5063-9.

40. Chu M, Hai W, Zhang Z, Wo F, Wu Q, Zhang Z, Shao Y, Zhang D, Jin L, Shi D. Melanin nanoparticles derived from a homology of medicine and food for sentinel lymph node mapping and photothermal in vivo cancer therapy. Biomaterials. 2016; 91: 182-99.

41. Wang X, Zhang J, Wang Y, Wang C, Xiao J, Zhang Q, Cheng Y. Multi-responsive photothermal-chemotherapy with drug-loaded melanin-like nanoparticles for synergetic tumor ablation. Biomaterials. 2016; 81: 114-24.